Journal of Applied Fluid Mechanics, Vol. 18, No. 9, pp. 2163-2179, 2025.
Available online at www.jafmonline.net, ISSN 1735-3572, EISSN 1735-3645.
https://doi.org/10.47176/jafm.18.9.3346

Multi-objective Optimization of Staggered Tube Banks in Cross-flow Using Machine Learning and Genetic Algorithm

A. Tamanaei[1], F. Kowsary[2], S. Sahamifar[3], and F. Samadi[4†]

[1] *Department of Mechanical Engineering, TU Darmstadt, Karolinenplatz 5, 64289 Darmstadt, Germany*
[2] *School of Mechanical Engineering, College of Engineering, University of Tehran, North Kargar St., Tehran, Iran*
[3] *Department of Mechanical, Industrial, and Mechatronics Engineering, Toronto Metropolitan University, Toronto, M5B 2K3, Canada*
[4] *Mechanical Engineering Dept., The University of Alabama, Tuscaloosa, AL, USA*

†*Corresponding Author Email: fsamadi@ua.edu*

ABSTRACT

This paper presents the numerical multi-objective optimization of staggered tube banks in cross-flow using neural networks and genetic algorithm. The objective is to determine the optimal dimensionless transverse and longitudinal pitches that establish a proper compromise between heat transfer enhancement and pressure drop minimization across a wide range of inlet Reynolds numbers (1,000–50,000). Tube banks simulations are performed for randomly selected pairs of design points to generate data on Nusselt number and friction factor. This dataset is used to train neural networks, which predict heat transfer and pressure drop characteristics as functions of dimensionless pitches. Appropriate objective functions are defined using trained neural networks and integrated into Genetic Algorithm to efficiently identify Pareto-optimal solutions. Results indicate that Reynolds number has a negligible effect on the Pareto front, as the optimal trade-offs between heat transfer and pressure drop remain consistent across different flow regimes. The *best* point on the Pareto front, defined as the solution with the minimum distance to the utopia point, exhibits dimensionless longitudinal and transverse pitches of approximately 0.90 and 1.30, respectively, regardless of the Reynolds number. Additionally, the study confirms that compact tube banks with dimensionless longitudinal pitches smaller than 1.0, often excluded in experimental and numerical studies, can be successfully simulated and optimized using the proposed framework. The findings provide practical guidelines for designing high-efficiency staggered tube banks and demonstrate a computationally efficient approach to optimize heat exchanger configurations without relying on empirical correlations.

Article History

Received January 5, 2025
Revised March 20, 2025
Accepted April 11, 2025
Available online July 5, 2025

Keywords:

Cross-flow staggered tube banks
Multi-objective optimization
Heat transfer
Genetic algorithm
Machine learning

1. INTRODUCTION

Cross-flow staggered tube banks are widely used in air conditioning systems, boilers, and electrical devices, where optimizing their thermal performance can significantly enhance system efficiency and reduce energy consumption. Due to their industrial relevance, numerous experimental and numerical studies have investigated their heat transfer and pressure drop characteristics to improve performance. Early empirical correlations, such as those proposed by Žukauskas (1972), provided fundamental insights into Nusselt number (*Nu*) variations and pressure drop coefficients over a wide range of Reynolds (*Re*) and Prandtl numbers. Subsequent experimental research, including Aiba et al. (1982), further explored the impact of *Re* number and dimensionless pitches on local *Nu* number and pressure drop coefficients. However, while these studies established foundational knowledge, they relied on empirical correlations that may lack accuracy for diverse geometric configurations and flow conditions.

The advent of computational methods enabled more detailed investigations into tube bank performance. Wilson and Bassiouny (2000) employed the finite volume method to numerically investigate heat transfer and pressure drop characteristics for one and two rows of tubes in the turbulent flow regime. Kim (2013) employed periodic and symmetric boundary conditions to investigate the effect of longitudinal pitch on the heat transfer in the in-line tube banks. His sensitivity analysis identified $k-\omega$ *SST* as the most accurate two-equation turbulent model

NOMENCLATURE

A	cross-sectional area	S_T	dimensionless transverse pitch
c_p	specific heat capacity	T	temperature
D	tube diameter	u	velocity component along x-axis
f	friction factor	v	velocity component along y-axis
G	goodness factor	V	velocity
h	convection coefficient	**Greek symbols**	
k	thermal conductivity of the fluid	ρ	density
ΔP	pressure drop along the computational periodic domain	μ	dynamic viscosity
$\overline{\Delta P}$	average pressure drop along the computational periodic domain	ζ	pressure drop coefficient
ΔT_i	inlet fluid and tubes wall temperature difference	θ	periodic dimensionless temperature
ΔT_{lm}	log-mean temperature difference	**Subscript and Superscript**	
ΔT_o	outlet fluid and tubes wall temperature difference	i	inlet
$\dot{m}$	inlet mass flow rate	L	longitudinal
Nu	*Nu* number	o	outlet
P_L	longitudinal pitch	t	total
P_T	transverse pitch	T	transverse
Q	heat transfer rate	w	wall
Re	*Re* number	opt	optimum
S_L	dimensionless longitudinal pitch	~	dimensionless parameter

for predicting heat transfer in in-line tube banks under symmetric and periodic boundary conditions. Later, Shah et al. (2013) employed the same methodology to investigate the pressure drop characteristics of staggered tube banks. Mohanty et al. (2018) performed a 2-D numerical study on in-line and staggered tube banks with three columns and five rows of tubes to determine heat transfer and pressure drop coefficients for forced convective heat transfer across different inlet *Re* numbers and dimensionless pitch values. Their study covered *Re* numbers ranging from 100 to 2,000 and dimensionless pitch values between 1.25 and 1.85, considering both elliptical and circular tubes. Abed and Afgan (2017) considered square and non-square configurations for in-line tube banks and numerically studied the effect of normalized pitches on heat transfer and flow characteristics, employing unsteady *Re*-averaged Navier-Stokes (URANS) turbulence models. Naik and Tiwari (2021a, b) analyzed fluid flow and heat transfer characteristics for circular tube banks with vortex generators using 3D numerical modeling in both in-line and staggered arrangements. Since heat transfer characteristics strongly depend on vortex generator placement, they varied the rectangular winglet pair positions relative to the tube centers to find the optimal configuration for maximizing heat transfer while minimizing pressure drop. Their study identified $\Delta x = 2$ and $\Delta y = \pm 1.25$ as the optimal vortex generator positions relative to the tube centers. In both studies, they subsequently, investigated the effect of attack angles of these rectangular winglet pairs on heat transfer characteristics, focusing on the best position identified in their previous research. Their study covered an inlet *Re* number range of 2,000 to 10,000 and attack angles from 15° to 60°. Li et al. (2019) conducted a 5-parameter numerical study to analyze heat transfer in twisted oval tube banks, utilizing symmetric and periodic boundary conditions with *Re* numbers ranging from 500 to 23,000.

Bejan (1995) demonstrated that optimum tube pitches exist to maximize heat transfer in tube banks under a fixed-volume constraint. Bejan et al. (1995) and Stanescu et al. (1996) extended this concept, optimizing these pitches for free and forced convective heat transfer, respectively, by varying the tube number density within a specified volume.

Matos et al. (2001, 2004a, b) performed experimental and numerical optimization of staggered tube banks with non-finned and finned elliptical and circular tubes in laminar flow using the finite element method. They employed the finite element discretization method for 2-D and 3-D numerical optimization, and determined the optimum tube pitches, elliptic tube eccentricity, and fin pitch that maximize heat transfer. Mainardes et al. (2007) later extended this work to the turbulent flow regime. However, since pressure drop was not considered in these studies, Mainardes et al. (2013) performed an optimization study to minimize pumping power for a finite number of tubes in the turbulent flow regime.

Many of the previously discussed studies focused on single-objective optimization, optimizing either heat transfer or pressure drop without considering their trade-off. Khan et al. (2007) utilized entropy minimization and previous analytical/experimental correlations to optimize in-line and staggered arrangements. Geb et al. (2013) combined volume-averaging theory and genetic algorithms to perform a 10-parameter optimization, using effectiveness as the objective function. Yilmaz and Yilmaz (2015) optimized tube number and pitches based on pressure drop and effectiveness, but they defined a fixed relationship between longitudinal and transverse pitches, limiting the design flexibility. Sahamifar et al.

(2019) used a generalized pattern search algorithm (GPSA) to numerically optimize staggered tube banks. They directly simulated a wide range of longitudinal and transverse pitches using symmetric and periodic boundary conditions. Rawa et al. (2021) numerically studied exergy and energy characteristics in twisted tube banks, introducing a novel arrangement and performing a multi-objective optimization on longitudinal and transverse pitches, *Re* number, and twist angle. Ge et al. (2021) performed a multi-objective shape optimization considering five tube shapes, treating 25 polar radii as design variables. It should be noted that Rawa et al. (2021) optimized only their proposed arrangement, while Ge et al. (2021) did not consider tube pitches as design variables.

All the studies mentioned above have performed a single-objective optimization on tube banks. Moreover, these studies, with the exception of the work carried out by Sahamifar et al. (2019), have used empirical correlations for *Nu* number and friction factor as the objective functions. It must be noted that empirical correlations could not accurately predict *Nu* number and friction factor in a wide range of Raynolds numbers and geometric parameters (Bacellar et al., 2016; Gu et al., 2017). This study employs CFD simulations through coupling MATLAB and ANSYS-Fluent to obtain *Nu* number and friction factor across a wide range of *Re* numbers (1,000–50,000), eliminating the inaccuracies associated with empirical correlations. It integrates ANNs as surrogate models and a multi-objective genetic algorithm (MOGA) to optimize tube pitches, significantly reducing computational costs.

Additionally, this study introduces a computational approach to simulate and optimize compact tube banks with dimensionless longitudinal pitches ≤ 1.0, a range that is rarely considered in prior research due to simulation constraints (Aiba et al., 1982; Yilmaz and Yilmaz, 2015; Gu et al., 2017; Rawa et al., 2021). In addition to obtaining the values of the objective functions using sub-scale CFD calculations, periodic and symmetric boundary conditions are utilized here, to preclude considering the entire domain of the tube bank, which reduces simulation time and computational cost significantly. As a result, a wide range of tube pitches could be simulated.

The novelty of this study lies in developing a CFD-based, data-driven framework for multi-objective optimization of staggered tube banks in turbulent cross-flow. Unlike prior works that relied on empirical correlations or single-objective formulations, this research simultaneously optimizes heat transfer and pressure drop using surrogate models trained on CFD data and evaluated via a MOGA. Additionally, it enables accurate modeling and optimization of compact tube banks with small dimensionless longitudinal pitches, which are rarely explored in prior studies due to simulation limitations. This study offers a generalized solution as the results demonstrate that the Pareto fronts and optimal configurations are largely invariant across a wide range of flow conditions.

This work sets a foundation for scalable, ML-driven optimization of thermal systems under realistic spatial and performance constraints. The findings of this study can be directly applied to real-world systems, particularly in the design of compact and energy-efficient heat exchangers, regardless of size. Staggered tube banks are widely utilized in industrial heat exchangers due to their ability to enhance heat transfer. By identifying Pareto-optimal configurations, this study provides insights that can help engineers design more compact and efficient heat exchangers, reducing both energy consumption and operational costs. Additionally, as the analysis and the optimization framework presented are scale-free, the outcome of the current paper can be easily generalized and integrated into HVAC systems and refrigeration systems design, power plants, and industrial applications to enhance their heat exchangers performance under various operating conditions and spatial limitations.

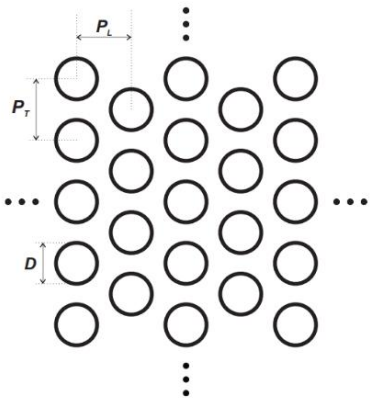

Fig. 1 Staggered tube banks

2. FLOW SIMULATION, NEURAL NETWORK TRAINING METHODOLOGY, AND OPTIMIZATION PROCESS

The problem domain with staggered tube banks is presented in Fig. 1, schematically. P_L, P_T, and D represent longitudinal pitch, transverse pitch, and tubes diameter, respectively.

Changing the longitudinal and transverse pitches significantly affects the fluid flow regime between the tubes. Since heat transfer and pressure drop characteristics are strongly dependent on the flow regime, variations in these pitches directly influence both characteristics. In this study, the dimensionless longitudinal and transverse pitches are treated as design variables in the optimization process. The *Nu* number and friction factor are considered as representative measures of heat transfer and pressure drop, respectively. Therefore, the variation of these characteristics with respect to the dimensionless pitches must first be determined. Based on this analysis, appropriate objective functions can be defined, and the optimization can then be carried out to identify the optimal trade-offs between heat transfer and pressure drop for each *Re* number. The details of this process are fully described in the following sections.

2.1 Parameters and Data Reduction

To determine the optimal compromises between the pressure drop and heat transfer characteristics with respect to the inlet *Re* number, it is appropriate to use the inlet

velocity as a reference parameter. The inlet *Re* number is defined as

$$\mathrm{Re}_i = \frac{\rho V_i D}{\mu} \tag{1}$$

where ρ, μ, and D are the density, viscosity of the fluid, and tubes diameter, respectively. Eq. (1) can be solved for the inlet velocity if the inlet *Re* number is known.

By knowing the inlet velocity, V_i, the inlet mass flow rate is calculated using

$$\dot{m} = \rho V_i A_i \tag{2}$$

where A_i is the inlet cross-sectional area which can be approximated as $P_T/2$. The pressure drop (ΔP) along the periodic computational domain is obtained by solving the continuity and momentum equations using the CFD package. The friction factor is then calculated based on the pressure drop across the periodic computational domain using

$$f = \frac{\Delta P}{\frac{1}{2}\rho V_i^2} \frac{A_i}{A_t} \tag{3}$$

where A_t is the total heat transfer surface, which, in the case of a two-dimensional simulation, is equal to πD.

Using CFD results, the total heat transfer rate is computed as

$$Q = \dot{m} c_p \left(T_0 - T_i\right) \tag{4}$$

where T_i, T_o are inlet and outlet bulk temperatures, and C_p is the specific heat capacity. T_o is an unknown parameter that can be calculated using dimensionless periodic temperature (θ), at the outlet, which is defined by the following equation and is obtained as a CFD simulation result

$$\theta_o = \frac{T_w - T_o}{T_w - T_i} = \frac{\Delta T_o}{\Delta T_i}. \tag{5}$$

In Eq. (5), T_w is the temperature of the wall of the tubes, which is assumed to be constant at $400\,K$ for the simulation. After calculating the total heat transfer rate, the convection coefficient can be determined using

$$h = \frac{Q}{A_t \Delta T_{lm}} \tag{6}$$

where ΔT_{lm} is the log-mean temperature difference defined as

$$\Delta T_{lm} = \frac{\Delta T_i - \Delta T_o}{\ln\left(\frac{\Delta T_i}{\Delta T_o}\right)} \tag{7}$$

The *Nu* number can be computed using the convection coefficient as

$$Nu = \frac{hD}{k} \tag{8}$$

where k is the thermal conductivity of air. Objective functions are defined using the computed heat transfer and pressure drop characteristics to perform the optimization and determine the optimal trade-offs between these two competing objectives. According to Webb and Kim (2004), the most appropriate metric for evaluating the heat exchangers is the goodness factor (G).

$$G = \frac{J}{f^{\frac{1}{3}}}; and\ J = \frac{Nu}{\mathrm{Re}\,\mathrm{Pr}^{\frac{1}{3}}}$$

Thus, the first objective function (OF_1), related to normalized pressure drop, is defined as

$$OF_1 = \sqrt[3]{\frac{f}{f_{opt}}} \tag{9}$$

while the second objective function (OF_2), associated with normalized heat transfer, is expressed as

$$OF_2 = \frac{Nu_{opt}}{Nu} \tag{10}$$

In these definitions, f_{opt} and Nu_{opt} are the reference (optimal) values obtained from the single-objective optimization study by Sahamifar et al. (2019). Normalization of the objective functions results in making them comparable and gaining a better insight toward their optimal values in different *Re* numbers.

The study by Sahamifar et al. (2019) showed that by using dimensionless longitudinal and transverse pitches of $S_L \cong 1$ and $S_T \cong 1.3$ as design variables, the goodness factor is maximized across all considered *Re* numbers. The dimensionless pitches are defined as

$$S_L = \frac{P_L}{D} \text{ and } S_T = \frac{P_T}{D} \tag{111}$$

The optimal dimensionless pitches obtained from single-objective optimization are used in the current study to calculate the optimal values of the friction factor and *Nu* number, using the numerical model, for all three considered *Re* numbers. The recalculated optimal values are presented in Table 1. These values are then used to normalize the heat transfer and pressure drop characteristics, and to define the objective functions accordingly. The objective functions defined in Equations (9) and (10) offer the advantage of having output values on the same order of magnitude, which enhances the stability and effectiveness of the multi-objective optimization process.

2.2 Geometry, Mesh, Boundary Conditions

Empirical correlations are derived by interpolating and extrapolating large sets of experimental data, which can introduce significant errors. Moreover, none of the existing correlations account for dimensionless transverse

Table 1 Single-objective optimization results (Sahamifar et al., 2019); Same values for *Re* number are considered in the current study

Re number	Nu_{opt}	f_{opt}
1,000	57.11	5.35
15,000	272.92	1.39
50,000	616.32	0.78

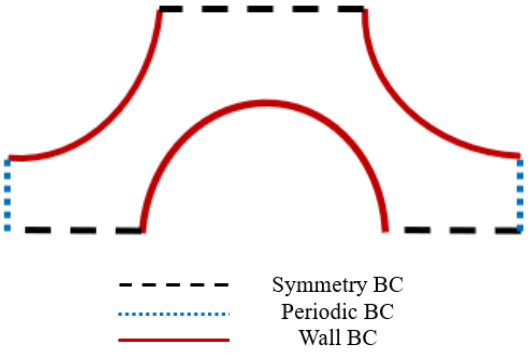

Fig. 2 Computational domain of tube banks

and longitudinal pitches smaller than 1.25, as experimental data for such small pitches are not available.

Considering this and given that the optimal point for single-objective optimization was found at very small pitch values (Sahamifar et al., 2019), CFD simulation becomes essential. Therefore, despite the existence of empirical correlations, detailed simulation is required to accurately capture the behavior at these compact configurations and to ensure that the neural network is trained on reliable, comprehensive data.

In the studies conducted by Kim (2013) and Sahamifar et al. (2019), periodic and symmetric boundary conditions were employed to significantly reduce simulation time and computational cost. Such assumptions for the boundary conditions are particularly suitable for modeling industrial-scale heat exchangers that contain more than 100 rows of tubes, where the influence of the first few tube rows on the overall performance is negligible. Since the accuracy of using these boundary conditions has been validated in the mentioned studies, they are adopted in the present work as well.

Although different tube arrangements in the computational domain shown in Fig. 1 can be considered with described boundary conditions, the specific configuration shown in Fig. 2 is used here. This arrangement, also employed by Sahamifar et al. (2019), enables the simulation of dimensionless longitudinal pitches smaller than 1, which are often excluded in experimental and numerical research due to modeling limitations. In this setup, symmetric boundary conditions are applied to the top and bottom boundaries, while periodic boundary conditions are applied to the left and right boundaries. The detailed boundary conditions applied are listed in Table 2.

To accurately predict flow characteristics in numerical simulations, careful mesh generation is essential, particularly near the tube walls where boundary layers develop. To properly resolve the boundary layer, the mesh must satisfy the constraint $y^+ < 1$, while there are no strict constraints on mesh resolution in other regions of the computational domain, aside from ensuring that mesh size remains appropriate for resolving global flow features. An unstructured triangular mesh is used throughout the computational domain, except in the

Table 2 Boundary conditions considered for the model

Boundary	Boundary Condition Type
Pipe Wall	$u = 0^*$ $v = 0^{**}$ $T = T_w = const.$
Control volume's upper and lower Boundaries (Symmetric)	$v = 0$ $T_w = 0$ $Q = 0$
Control volume's left and right boundaries (Periodic)	$u(x,y) = u(x + S_L, y)$ $p(x,y) = p(x + S_L, y) + \overline{\Delta p_t}$ $\theta = \frac{T(x,y) - T_w}{T_i - T_w}$ $T_i = \frac{\int_A T(\rho \vec{v} \overrightarrow{dA})}{\int_A (\rho \vec{v} \overrightarrow{dA})}$

* Velocity component along *x*-axis

** Velocity component along *y*-axis

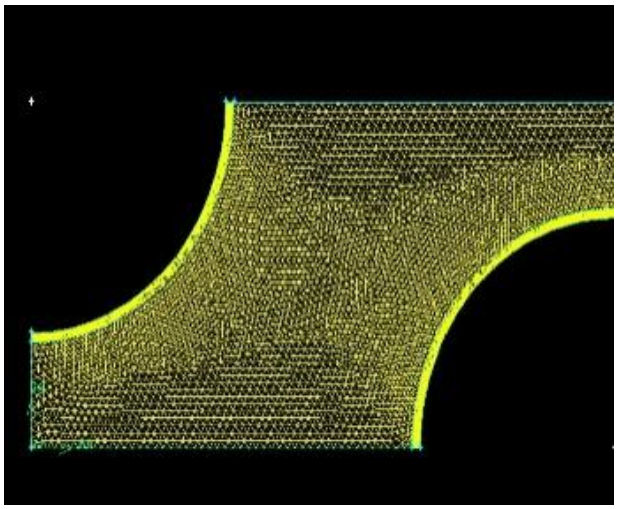

Fig. 3 Mesh used, shown for half of the computational domain

boundary layer region, where a more refined mesh is required. To meet the $y^+ < 1$ requirement, the boundary layer mesh is initially generated under critical conditions and then applied to other cases (Hoseinzadeh et al., 2020). According to the sensitivity analysis performed by Sahamifar et al. (2019), reducing the transverse pitch increases y^+ and vice versa, while changes in longitudinal pitch have a negligible effect on y^+. Based on their findings, the boundary layer mesh in this study is designed for the minimum longitudinal and transverse pitches and then reused for other pitch combinations in the optimization process. An example of the meshing scheme used in the computational domain is shown in Fig. 3.

After generating the boundary layer mesh for the critical pitch configuration, a mesh independence study was conducted to ensure that the CFD results are not sensitive to mesh size (Hoseinzadeh & Heyns, 2020; Nazarieh et al., 2023). This analysis was performed for the minimum and maximum inlet *Re* numbers (1,000 and

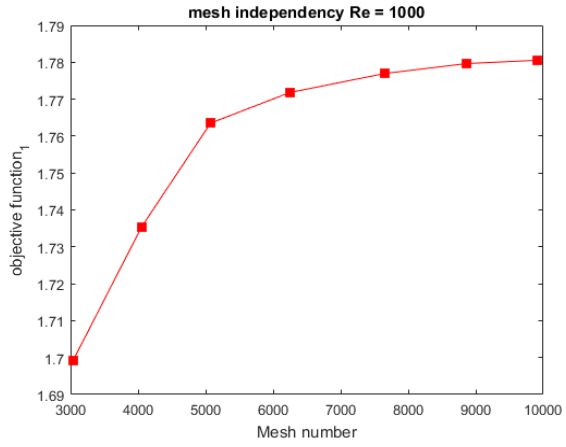

(a)

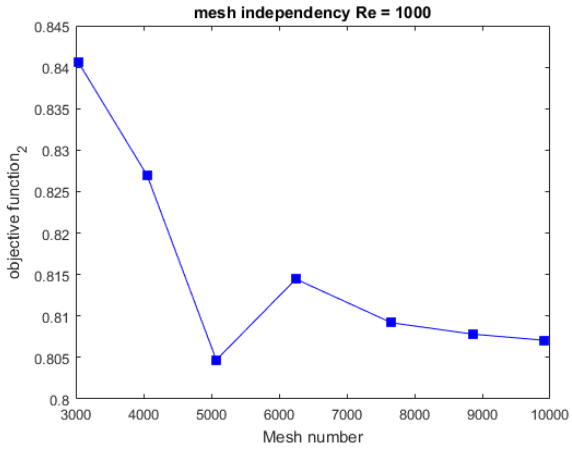

(b)

Fig. 4 Mesh independency results for the inlet *Re* number equal to 1000 and the worst case in design space ($S_L = 1.75$; $S_T = 1.1$), for a) first objective function, b) second objective function

Table 3 Design variables and their range

Design variables	Minimum	Maximum
S_L	0.9	4
S_T	1.1	4

50,000). The mesh independence study was carried out for $S_L = 1.75, S_T = 1.1$, and the results are shown in Figs 4 and 5. The results indicated that for mesh counts greater than 6,248 and 12,334, at *Re* numbers of 1,000 and 50,000 respectively, the variations in friction factor and *Nu* number were less than 1%. Based on these findings and given that the $y^+ < 1$ constraint is also satisfied, this meshing scheme was applied to all simulations involving dimensionless pitch values within the range specified in Table 3.

The lower bounds of the design variables were selected as 0.9 for longitudinal pitch and 1.1 for transverse pitch, since tube banks with dimensionless pitches below these values cannot be simulated as tubes will collide.

It is evident that satisfying the $y^+ < 1$ constraint for each pair of pitches using customized meshes would minimize the total mesh count for that specific case. However, implementing this approach is practically

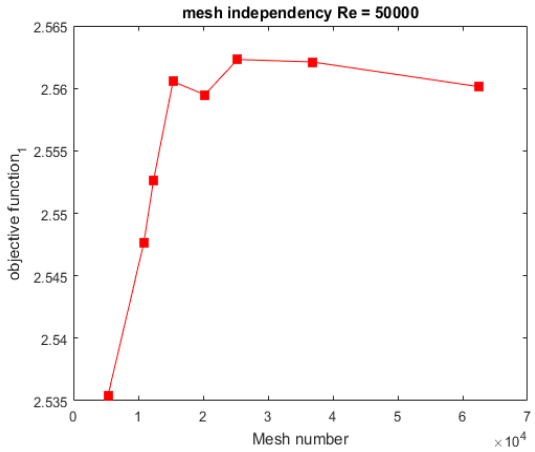

(a)

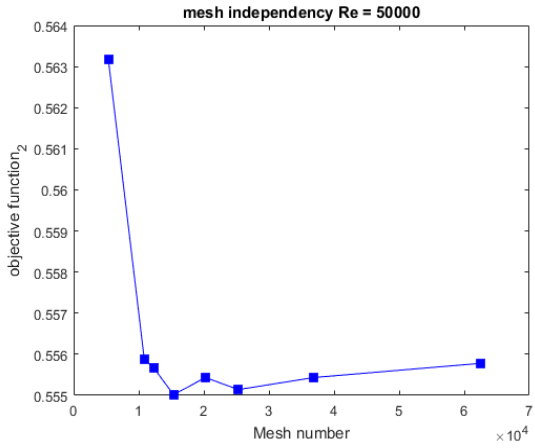

(b)

Fig. 5 Mesh independency results for the inlet *Re* number equal to 50,000 and the worst case in design space ($S_L = 1.75$; $S_T = 1.1$) for a) first objective function, b) second objective function

infeasible, as a large number of simulations are required to generate sufficient data for training the neural networks. To obtain the heat transfer and pressure drop characteristics, the discretized forms of the continuity, momentum, and energy equations were solved using the second-order upwind scheme within ANSYS-Fluent.

In this study, air at an inlet temperature of 288.15 K is used as the working fluid. Since the Mach number of the inlet flow is below the critical threshold, the flow is assumed to be incompressible. The thermophysical properties of the inlet fluid are provided in Table 4.

Table 4 Thermophysical properties of inlet fluid

Thermophysical properties	Air
Inlet bulk temperature, T_i (K)	288.15
Density, ρ $(\frac{kg}{m^3})$	1.2167
Specific heat capacity, c_p $(\frac{J}{kg\,K})$	1006.763
Viscosity, μ $(\frac{kg}{m\,s})$	1.78675×10^{-5}
Thermal conductivity, k $(\frac{W}{m\,K})$	0.025352

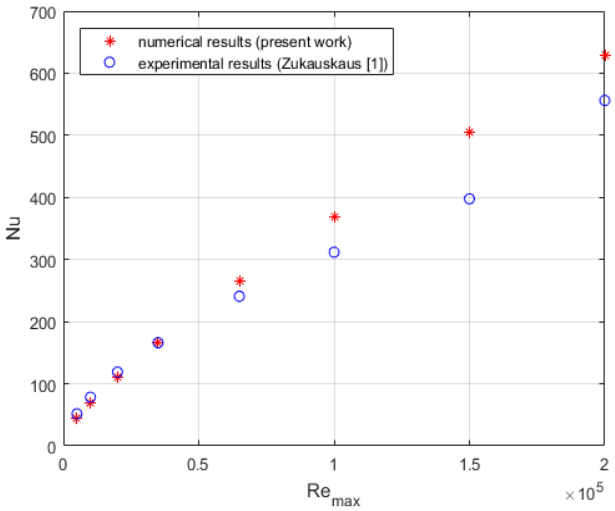

Fig. 6 Comparison of heat transfer characteristics resulting of the numerical simulation with experimental study (Zukauskaus, 1972) for air with Prandtl number = 0.71 and $S_L = S_T = 1.5$

Based on Kim (2013), Kariman, et al. (2023), and Sahamifar et al. (2019), $k-\omega$ *SST* model is employed as flow conditions of the problem investigated in the current study are similar to those. For the sake of simplification, it is assumed that the tube length is much greater than the diameter; therefore, all governing equations are solved in two dimensions (2-D). The SIMPLE algorithm is used to couple velocity and pressure fields.

According to the sensitivity analysis conducted by Sahamifar et al. (2019), setting the convergence criterion for the energy equation below 10^{-7} does not significantly influence the results. Based on this finding, the convergence criteria were set to 10^{-6} for the residuals of all equations except the energy equation, for which a more stringent criterion of 10^{-7} was applied.

2.3 Model Validation

As mentioned previously, the inlet velocity is considered the reference velocity in this study. The variation of the *Nu* number with *Re* number is commonly used to validate numerical models, as shown in studies by Deng et al. (2024) and Karali et al. (2025). In this work, validation is performed for various maximum *Re* numbers using dimensionless pitches of $S_L = S_T = 1.5$. The results of this validation are compared with the experimental data of Zukauskas (1972), one of the most widely cited studies in the literature.

Figure 6 shows that the heat transfer characteristics predicted by the numerical model follow a trend similar to the experimental data. As seen in the figure, for *Re* numbers below 40,000, the deviation between the numerically computed *Nu* number and the experimental values is negligible. This deviation increases when the *Re* number ranges from 65,000 to 150,000. However, for *Re* numbers between 150,000 and 200,000, the deviation decreases again, which corresponds to a change in the correlation coefficients proposed by Zukauskas (1972). It must be noted that empirical correlations do not necessarily predict the pressure drop for all *Re* numbers accurately (Bacellar et al., 2016; Gu et al., 2017).

Potential sources of error in the CFD simulation include two-dimensional (2D) modeling of the flow, particularly in the turbulent regime, meshing efficiency across different geometric configurations and *Re* numbers, and the application of periodic boundary conditions. Among all these cases, only the use of periodic boundary conditions for small row counts could introduce noticeable deviations from the actual performance as real-world configurations with finite tube banks may exhibit inlet and outlet effects that are not captured in a fully periodic domain. However, since the optimization trends are determined by the relative performance of different configurations, rather than absolute performance values, these potential errors do not significantly alter the optimal tube bank design. The low-fidelity meshing and 2D modeling choices have been verified to have a minimal impact on the accuracy of the Pareto-optimal solutions.

At this step, neural networks are employed to develop surrogate models for predicting heat transfer and pressure drop characteristics based on the dimensionless pitches, which serve as the design variables. These surrogate models significantly simplify the optimization process by eliminating the need for repeated CFD simulations. The following section briefly outlines the procedure used to construct and apply these models in the optimization framework.

2.4 Neural Network Model

A neural network consists of multiple layers, each containing a set of neurons. The first and last layers are referred to as the input and output layers, respectively. Between them are one or more hidden layers, which contain several neurons and are responsible for processing the input data. Each neuron in the input layer receives one of the design variables. These inputs are then processed through the hidden layers, and the neurons in the output layer produce the predicted value for the target output.

All neurons in the network are fully connected, meaning there is communication between every neuron in one layer and each neuron in the next layer. Data is passed forward by multiplying the outputs of neurons in one layer by a matrix of values known as weights. The result is an array, to which another array, called the bias, is added. Each layer in the network has its own weight matrix and bias vector, which are adjusted during the training process. The training phase involves finding the optimal values of these weights and biases so that the network can accurately map inputs to the desired outputs.

After completing the described computations, the resulting array of values is passed through an activation function. This function determines whether a neuron should be activated based on the input it receives. Activated neurons pass their outputs to the next layer, continuing the process. This mechanism of transferring data from the input layer to the output layer is known as forward propagation.

In each training iteration, the predicted output from forward propagation is compared with the actual target

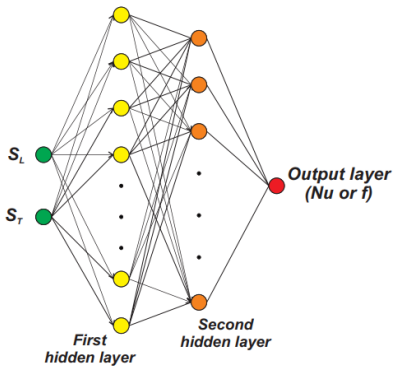

Fig. 7 Architecture of neural networks used

Table 5 Features of neural networks used for *Nu*

Parameter	No. neurons	Activation function
Prim. hidden layer	72	tanh
Secon. hidden layer	36	tanh
Output layer	1	linear

Table 6 Features of neural networks used for *f*

Parameter	No. neurons	Activation function
Prim. hidden layer	80	tanh
Secon. hidden layer	40	tanh
Output layer	1	linear

value, and the difference (error) is computed. This error is then used to calculate the mean squared error (MSE), which quantifies the overall prediction accuracy of the network (Fausett, 2006).

In the next step, the computed differences between the predicted and actual values are propagated back to the input layer through a backpropagation process. This step adjusts the weight matrices and bias arrays across the network to reduce errors and improve prediction accuracy. These forward and backward passes are repeated iteratively until the network reaches the desired level of accuracy in predicting the output values.

To further improve training efficiency and generalization, Bayesian regularization is applied. Networks using this technique tend to be more robust, and the method can significantly reduce—or even eliminate—the need for a separate validation dataset (Burden and Winkler, 2008). Therefore, Bayesian regularization-backpropagation is used in this study to regularize the networks and minimize training error.

Two separate neural networks—one for predicting the *Nu* number and the other for the friction factor—are trained for each *Re* number. Each network consists of two hidden layers. If the number of hidden layers or neurons is insufficient, the network will fail to capture the complexity of the input–output relationship. Conversely, using more neurons or layers than necessary can lead to overfitting, where the network performs well on training data but poorly on unseen cases. Thus, the minimum network size that ensures the required accuracy is employed. According to Fausett (2006), a neural network with two hidden layers can approximate any regression function to any desired level of accuracy, and as shown in Section 3.2, the architectures used in this study achieve the required accuracy effectively.

The neural networks are trained to replace computationally expensive CFD simulations during the optimization process. CFD solutions require significant computational time to converge, whereas a trained neural network can predict results nearly instantaneously. The architecture used for the networks is illustrated in Fi. 7. The input layer includes two neurons, one for the dimensionless longitudinal pitch and the other for the dimensionless transverse pitch. The output layer predicts either the *Nu* number or the friction factor. Various activation functions were tested for the hidden layers, and the best-performing functions were selected for each case. The characteristics of the trained neural networks for the two objective functions are summarized in Tables 5 and 6.

Once the neural networks are trained, the multi-objective optimization can be performed. A MOGA is used for this purpose. The details and features of the algorithm are described in the next section.

2.5 Genetic Algorithm

In engineering applications, the goal is typically to find the global optimum; however, deterministic search methods can sometimes become trapped in local optima. In such cases, stochastic optimization methods are preferred. In this study, a genetic algorithm (GA) is employed to perform multi-objective optimization and determine the optimal trade-offs between the friction factor and the *Nu* number. The genetic algorithm is selected due to its accuracy, efficiency, and stochastic nature that make it well-suited for multi-objective optimization problems, particularly those involving ML models.

The genetic algorithm simulates the principles of biological evolution, such as selection, crossover, and mutation, allowing more promising (i.e., "fitter") individuals to dominate over weaker ones. To simulate this evolutionary process, the objective function values for each individual in the population must be evaluated. However, because direct evaluation using CFD simulations is time-consuming, the surrogate models (neural networks) trained in the previous section are used to predict objective function values, thereby significantly reducing computational cost.

The optimization process using the genetic algorithm proceeds as follows: First, an initial population of 2,000 individuals is randomly generated. A relatively large population size is chosen to ensure that the obtained optimal solutions are robust and not sensitive to the population size. Next, the objective functions are evaluated for each individual. Then, this population will identify the fittest individuals using the tournament method (Fang & Li, 2010) to parent next-generation individuals. The crossover fraction determines the number of offspring created through recombination of parent

Table 7 Specifications of the utilized multi-objective genetic algorithm

Specifications	Value
Population size	2000
Tournament size	2
Crossover fraction	0.8
Migration fraction	0.2
Migration interval	20
Function tolerance	1e-4
Constraint tolerance	1e-3
Pareto front population fraction	0.35

individuals. The remaining individuals are generated through mutation, which introduces small random changes using a random number generator. Additionally, a migration operator is applied to further enhance the population. The population is divided into subpopulations, and the worst-performing subpopulation is periodically replaced with the best-performing one, based on a predefined migration interval.

The optimization process is terminated based on one or more of the following criteria: the maximum number of generations, time limit, fitness threshold, constraint tolerance, or function tolerance. The specific parameters and settings used for the genetic algorithm in this study are summarized in Table 7.

The process of CFD simulation, ML, and optimization are illustrated in Figures 8 and 9. In this study, 300 simulations are performed for each *Re* number, resulting in a total of 900 simulations which are used to train the neural networks. Due to the large number of required simulations, it was not feasible to manually create the geometry, generate the mesh, and set up ANSYS Fluent cases for every pair of design variables. Therefore, the entire simulation and data collection workflow was automated by coupling MATLAB with ANSYS Fluent.

3. RESULTS AND DISCUSSIONS

In the following sections, the variation of heat transfer and pressure drop characteristics with respect to the dimensionless pitches is first presented. This is followed by the results of neural network training and the multi-objective optimization process.

3.1 Simulation Results

For each *Re* number considered in this study, 300 random combinations of dimensionless longitudinal and transverse pitches, uniformly distributed throughout the design space, were simulated. The resulting variations in the friction factor and *Nu* number with respect to these dimensionless pitches are shown in Figs 10 and 11.

The pressure is highest at the stagnation point. It decreases while the velocity increases as the flow moves along the surface of the cylinder. This behavior is influenced by the development of the boundary layer. As the boundary layer grows, flow separation occurs. This leads to the formation of vortices behind the cylinder, which enhance heat transfer.

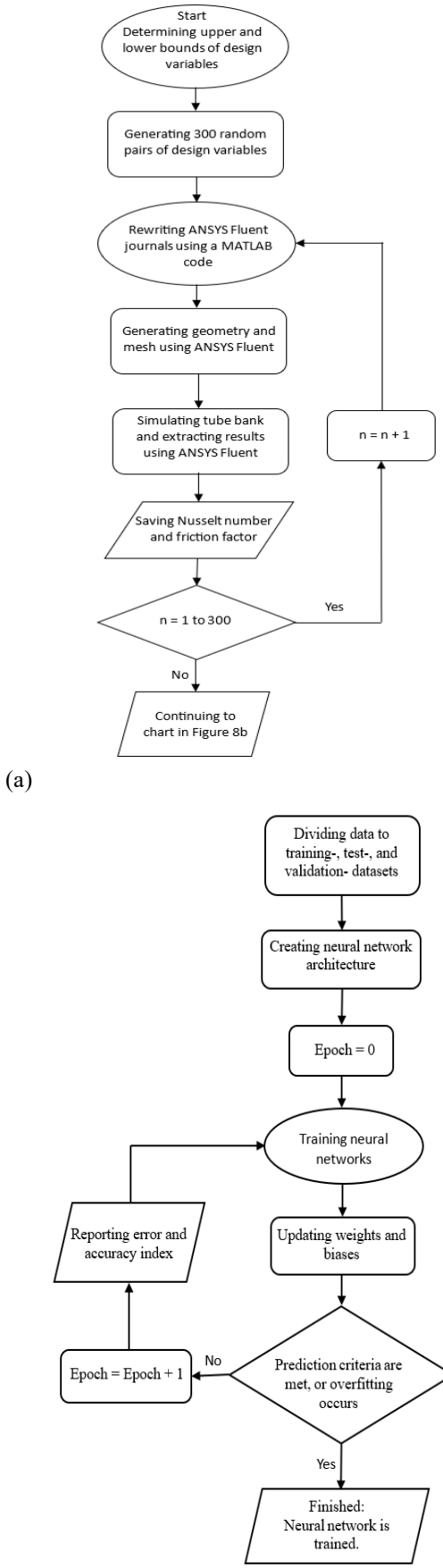

Fig. 8 Process of CFD simulation and ML for each *Re* number, a) Dataset creation process diagram, b) Neural network training process diagram

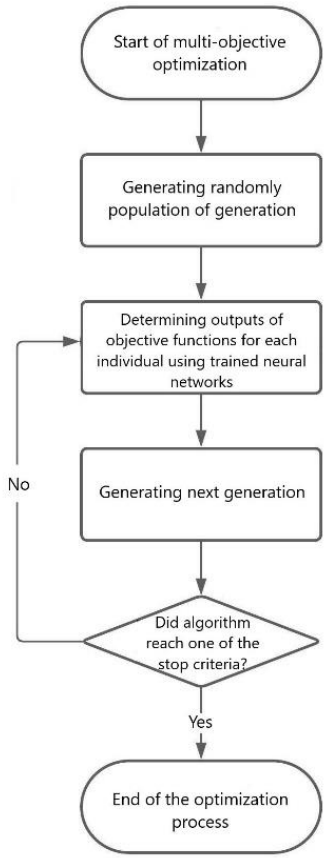

Fig. 9 Process of optimization

The transition from a laminar to a turbulent boundary layer increases turbulence, promoting better mixing and higher heat transfer. However, the turbulent boundary layer also results in increased drag and alters the pressure distribution, especially in the wake region. These effects significantly influence both heat transfer and pressure drop along the cylinder.

As illustrated in Figures 10 and 11, the overall trend of variation in these characteristics with respect to the dimensionless pitches is not significantly influenced by the *Re* number. However, it is observed that the Nusselt number increases and the friction factor decreases as the *Re* number increases. Additionally, both the *Nu* number and friction factor increase as the dimensionless pitches decrease, and vice versa. These observations confirm that the dimensionless longitudinal and transverse pitches have a significant impact on the thermal and hydraulic performance of the tube banks. Thus, they play a critical role in the design optimization process and must be carefully considered as key design variables.

3.2 Neural Network's Training Results

After simulating the tube bank, the results for each *Re* number are randomly divided into three datasets: the training dataset, the test dataset, and the validation dataset. These datasets contain 68%, 17%, and 15% of the total data, respectively. In total, 85% of the data (training + test) for each *Re* number is used to train and test the neural networks developed for predicting the friction factor and

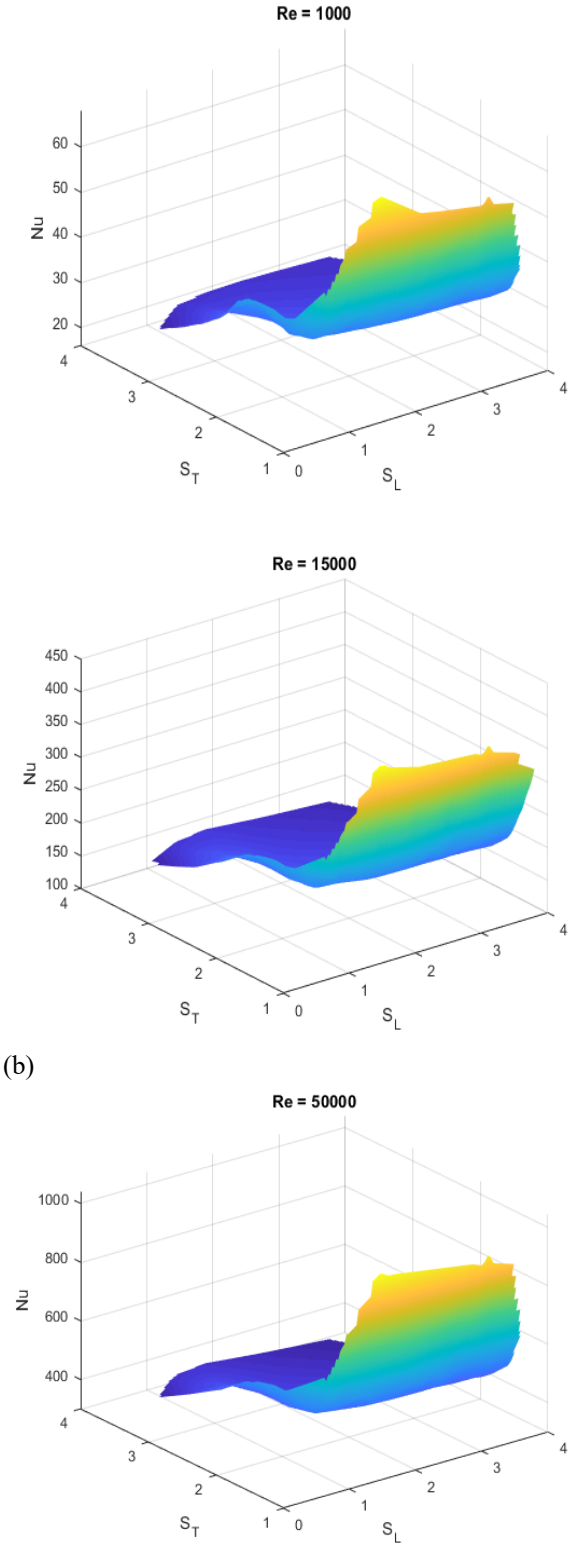

(b)

(c)

Fig. 10 Variation of *Nu* number with dimensionless pitches for each *Re* number, a) *Re* = 1000, b) *Re* = 15000, and c) *Re* = 50000

the *Nu* number. To ensure the accuracy and optimality of the neural networks, it is essential to perform hyperparameter tuning on unseen data (Mashhadi et al., 2024). This tuning process is carried out using the test dataset, which contains 17% of the data. Following this, the generalization capability and prediction accuracy of

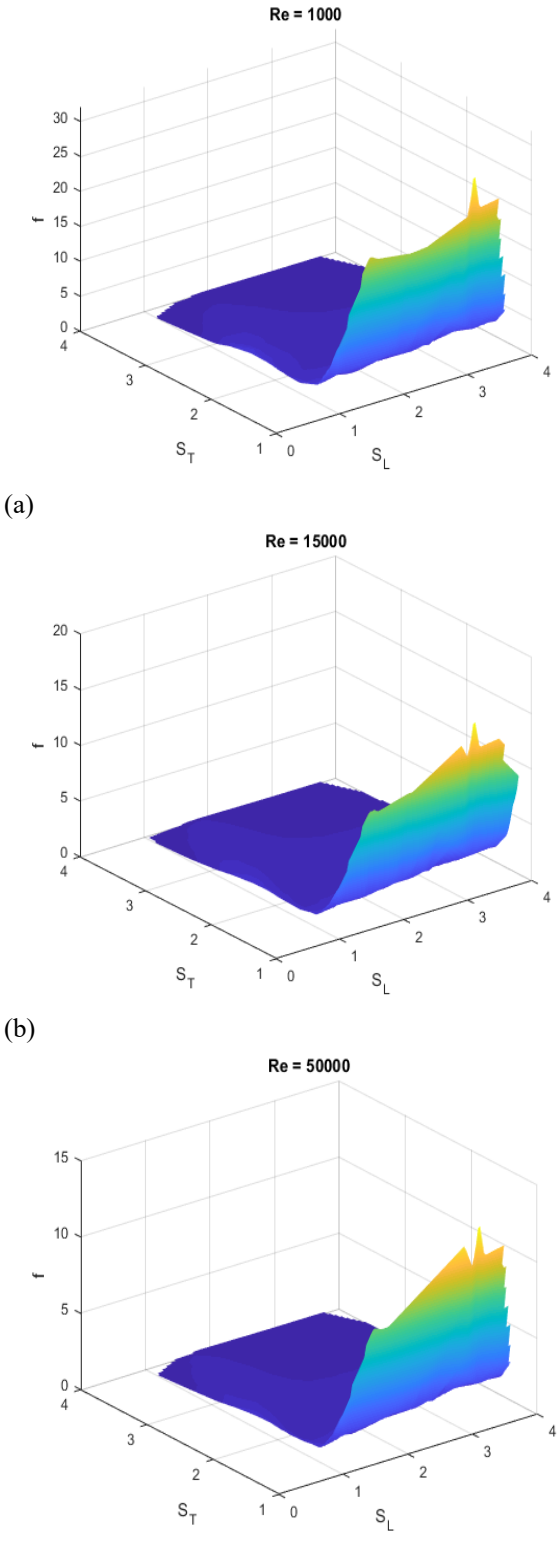

Fig. 11 Variation of friction factor (f) with dimensionless pitches for each *Re* number, a) *Re* = 1000, b) *Re* = 15000, and c) *Re* = 50000

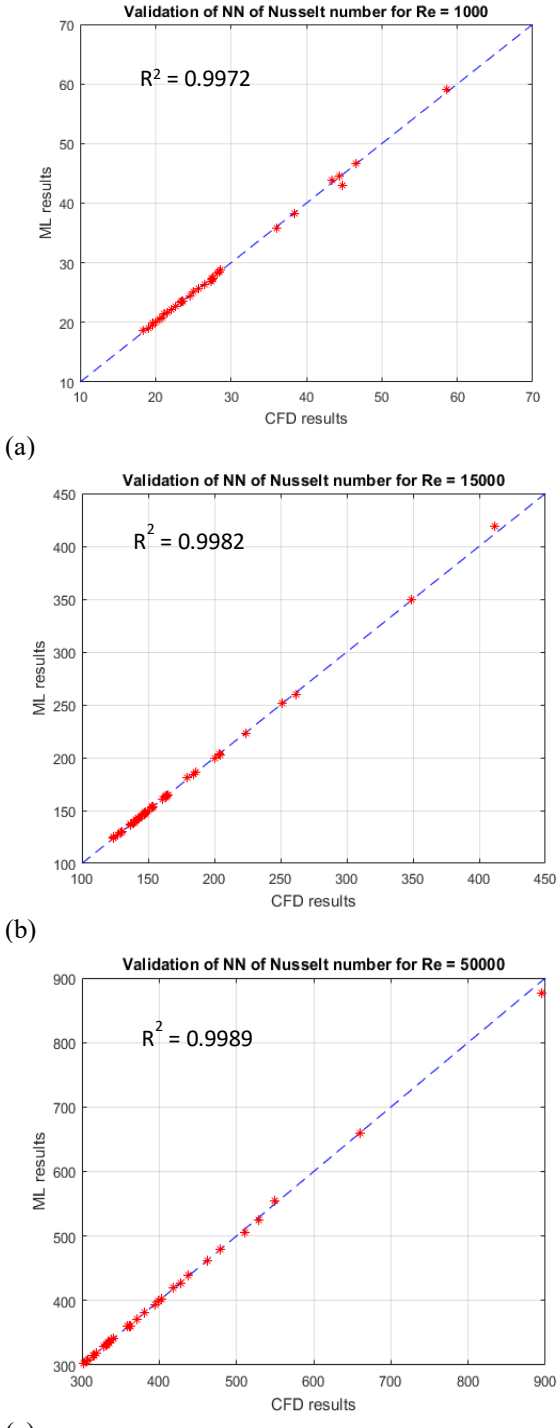

Fig. 12 Validation of neural network of *Nu* number, against CFD results for each *Re* number a) *Re* = 1000, b) *Re* = 15000, and c) *Re* = 50000

the trained networks are evaluated by calculating the coefficient of determination (R^2) using data in the validation dataset.

As shown in Figs 12 and 13, the trained neural networks exhibit excellent accuracy. The ML results shown in these figures represent the predicted values obtained from the trained networks. Furthermore, these figures help eliminate concerns of overfitting, as the validation dataset was not involved in the training process.

During the training of neural networks, it is essential to monitor learning curves, which are updated after each training iteration. These curves compare the prediction error for both the training and test datasets. Since the weights and biases are optimized using the training dataset, the training error curve typically shows a monotonic decrease. However, if the test error curve

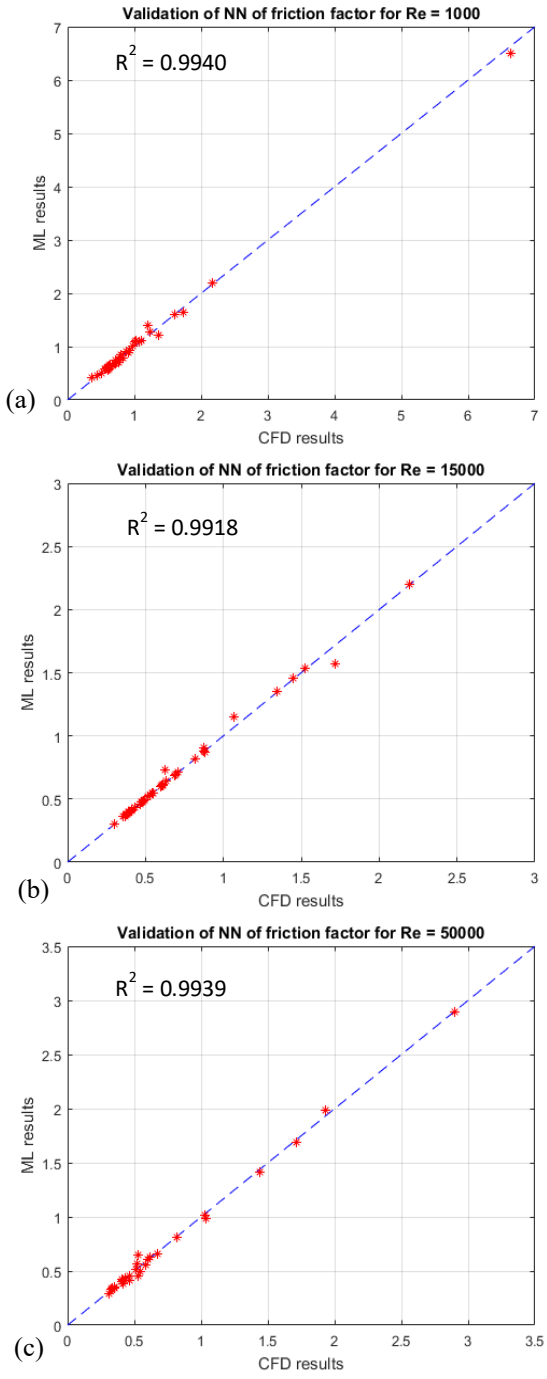

Fig. 13 Validation of neural network of friction factor against CFD results for each *Re* number a) *Re* = 1000, b) *Re* = 15000, and c) *Re* = 50000

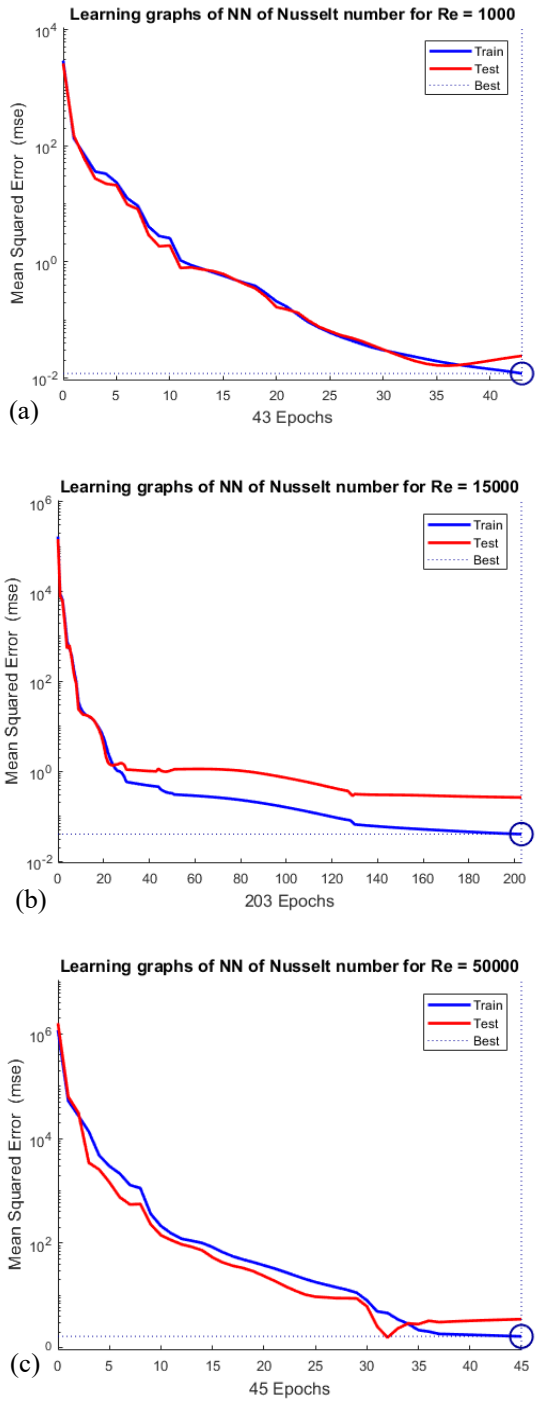

Fig. 14 Learning graphs of *Nu* number's neural network for each *Re* number, showing mean squared error versus the number of epochs for a) *Re* = 1000, b) *Re* = 15000, and c) *Re* = 50000

training and test error curves widens, this is an indication of overfitting, and the training process should be terminated.

The learning curves for predicting the friction factor and *Nu* number at each *Re* number are presented in Figs 14 and 15. At this stage, the trained neural networks can accurately predict the *Nu* number and friction factor based on the dimensionless pitches for the considered *Re* numbers with significantly reduced computation time and cost compared to full CFD simulations.

3.3 Optimization Results

Optimizing a system considering only one design variable often results in changes in other design variables, which cause efficiency reduction. Moreover, the effect of the optimization will be reduced or eliminated. Therefore, a trade-off must be established between competing design objectives. For this reason, multi-objective optimization methods have gained increasing attention over the past two decades. The aim of this study is to identify the

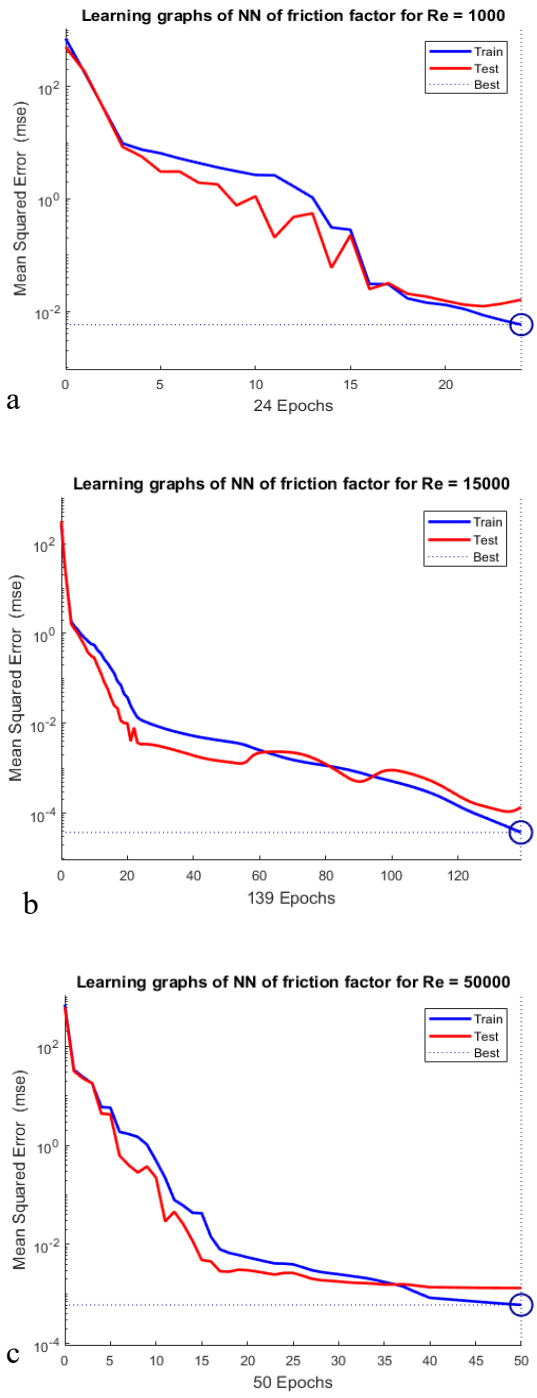

Fig. 15 Learning graphs of friction factor's neural network for each Re number showing mean squared error versus the number of epochs for a) Re = 1000, b) Re = 15000, and c) Re = 50000

optimal compromise between heat transfer and pressure drop by varying the dimensionless pitches between the tubes, within the range of *Re* numbers specified in Table 1. In other words, the goal is to configure the tube bank such that the fluid experiences minimal pressure drop while achieving maximum heat transfer during flow through the system.

Pareto fronts obtained through the optimization of the objective functions are shown in Fig. 16. As illustrated,

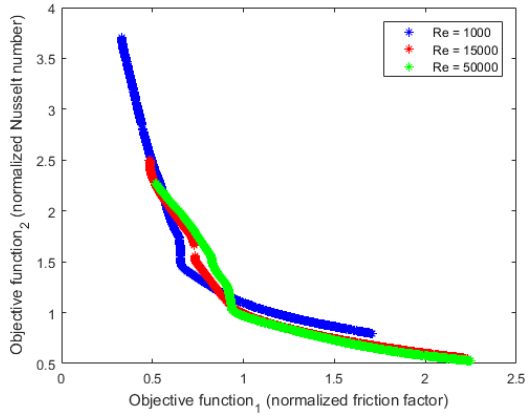

Fig. 16 Pareto fronts resulting from optimization of objective functions for each *Re* number

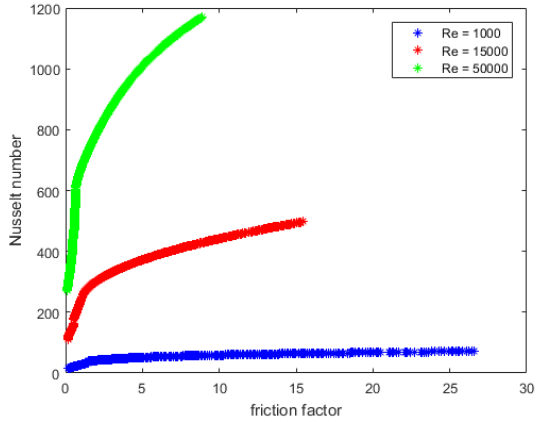

Fig. 17 *Nu* number versus pressure drop for each *Re*

the *Re* number has only a slight effect on the Pareto fronts, and the curves are very close to one another. It can also be concluded from this figure that there are certain normalized *Nu* numbers and friction factors, located below the normalized Pareto fronts, that cannot be achieved at any *Re* number. In other words, the tube bank efficiency has an upper bound that cannot be exceeded.

To better visualize the effect of *Re* on the trade-off between heat transfer and pressure drop, the normalized characteristics are transformed into unnormalized characteristics, yielding a new curve for each *Re* number. These curves, which show the variation of *Nu* number versus pressure drop, are presented in Fig. 17. As expected, with increasing *Re*, the Pareto frontier includes points with higher *Nu* numbers and lower friction factors. For each *Re*, there exists a point referred to as the *utopia* point, theoretical and ideal, where the *Nu* number is maximized, and the friction factor is minimized, simultaneously corresponding to the minimum values of both objective functions. This point lies below the Pareto frontier, meaning it is unattainable in practice.

The Pareto curve is known as a tradeoff curve. None of the points on the Pareto front are preferred to other points. The *best* point is the point that provides a balance or optimal compromise between different objective functions. Ideally, it is a single selected point with the closest distance to the eutopia point, which results in the

Table 8 Comparison of best point specification of present work with single-objective optimization (Sahamifar et al., 2019)

Re	Present work				Single-objective optimization	
	S_L	S_T	OF_1	OF_2	S_L	S_T
1000	0.90	1.31	0.82	1.26	0.94	1.22
15,000	0.90	1.33	0.97	1.01	0.98	1.27
50,0000	0.90	1.47	0.96	1.00	1.03	1.35

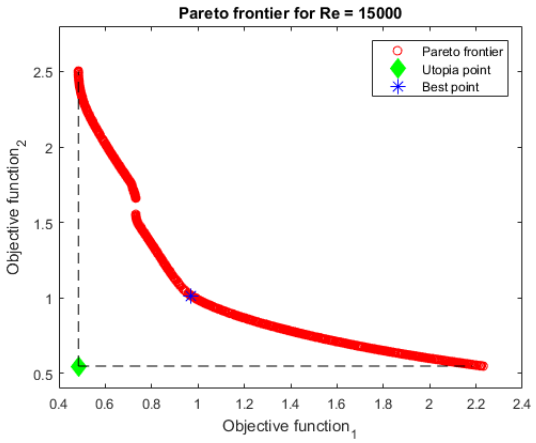

Fig. 18 Utopia and best point for *Re* number equal to 15,000

best possible solution. Selecting the *best* point is particularly effective when the Pareto front is convex (Belegundu & Chandrupatla, 2019).

As an example, the *utopia* point and the *best* point for Re = 15,000 are illustrated in Fig. 18. After comparing the dimensionless pitches corresponding to the *best* points for all *Re* numbers, it is observed that *Re* has no influence on the optimal pitch values. The dimensionless pitches and corresponding objective function outputs for the *best* point at each *Re* number are summarized in Table 8.

According to Table 8, the dimensionless pitches resulting from *best* point of the multi-objective optimization are close to those resulting from the single-objective optimization. OF_1 and OF_2 represent the values of the two considered objective functions. Since these functions are defined using the heat transfer and pressure drop characteristics derived from the single-objective optimization results, the values of OF_1 and OF_2 for the single-objective case are equal to 1.

Finally, to validate the obtained Pareto fronts, fifty points from the Pareto frontier corresponding to Re = 15,000 were selected and used as the initial generation for the MOGA. The algorithm then performed one optimization iteration for these points using the CFD package directly, instead of relying on the neural network. The accuracy of the surrogate model was approved as the results showed no difference between the Pareto fronts obtained from the neural network model and those from the CFD-based evaluation.

Contours of temperature, pressure, and velocity for the best point on the Pareto frontier at *Re* = 15,000 are presented in Fig. 19. The temperature contour illustrates

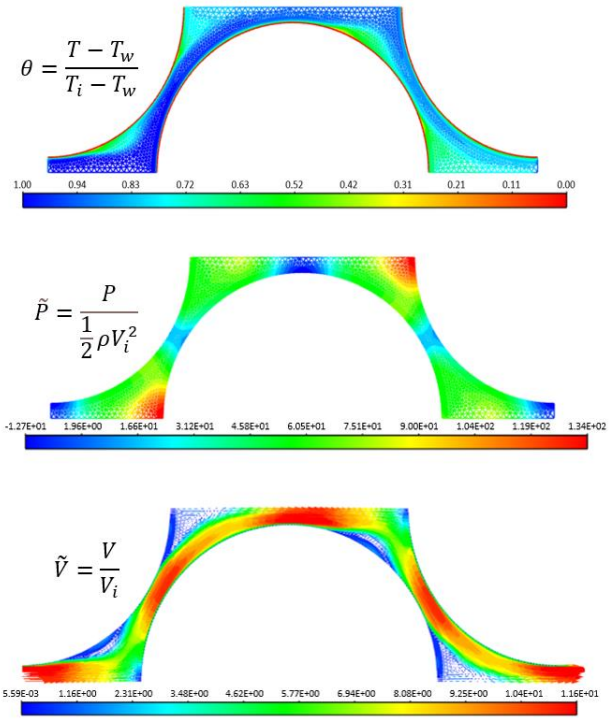

Fig. 19 Contours of dimensionless temperature, pressure, and velocity of the best point on the Pareto frontier for *Re* = 15,000 ($S_L \cong 0.9$; $S_T \cong 1.37$)

that the fluid temperature increases as it flows through the tube bank. Additionally, the velocity contour indicates that the numerical model successfully captures vorticity and flow separation regions. By comparing the velocity and pressure contours, it can be observed that velocity increases in regions where pressure decreases, as expected based on fundamental fluid dynamics principles.

4. CONCLUSION

A numerical multi-objective optimization was carried out to identify optimal trade-offs between heat transfer and pressure drop characteristics for staggered tube banks operating in the turbulent flow regime. The influence of the inlet *Re* number on these trade-offs was also investigated. Unlike previous studies that relied on empirical correlations for estimating heat transfer and friction factor, this study defined two independent objective functions, enabling a more accurate and flexible optimization process. As highlighted by Bacellar et al. (2016) and Gu et al. (2017), empirical models often fail to capture heat transfer and pressure loss behavior accurately over a wide range of *Re* numbers and geometric

configurations. Optimization has been performed by simulating the heat transfer and flow for three *Re* numbers and some randomly generated design variables. To prevent simulation of the entire domain of the tube bank and reduce convergence time and computational cost, periodic and symmetric boundary conditions have been employed. Afterwards, the relations between these characteristics and dimensionless pitches have been modeled using the neural network, which served as surrogate models to eliminate the need to use empirical correlations and CFD. Optimized equilibriums between considered characteristics were extracted using multi-objective genetic algorithm. The results show that Pareto fronts achieved from optimization of defined objective functions are extremely close, and the inlet *Re* number has no significant effect on these curves. The *best* points on Pareto fronts also have approximately the same dimensionless pitches ($S_L \cong 0.9$; $S_T \cong 1.37$).

The proposed framework can be extended to other geometries, such as inline tube banks, finned tubes, and novel cross-flow heat exchanger designs, to optimize their performance for various industrial applications, regardless of the size and the inlet *Re* number. Additionally, applying this methodology to different working fluids may offer further insights into flow and heat transfer characteristics. The model also holds potential for adaptation to multiphase flow applications, including boiling, condensation, high-temperature/high-pressure environments, and variable inlet conditions.

CONFLICT OF INTEREST

There is no conflict of interest to disclose.

AUTHORS CONTRIBUTION

Tamanaei: Modeling; Data analysis; Writing, initial draft. **Kowsary:** Conceptualization; Supervision; Writing, review and revision. **Sahamifar:** Modeling, Writing, initial draft. **Samadi:** Supervision; Writing, review and revision.

REFERENCES

Abed, A., & Afgan, I. (2017). A CFD study of flow quantities and heat transfer by changing a vertical to diameter ratio and horizontal to diameter ratio in inline tube banks using URANS turbulence models. *International Communications in Heat and Mass Transfer*, *89*, 18–30. https://doi.org/10.1016/j.icheatmasstransfer.2017.09.015

Aiba, S., Tsuchida, H., & Ota, T. (1982). Heat transfer around tubes in staggered tube banks. *Bulletin of JSME*, *25*(204), 927–933. https://doi.org/10.1299/JSME1958.25.927

Bacellar, D., Aute, V., Huang, Z., & Radermacher, R. (2016). Airside friction and heat transfer characteristics for staggered tube bundle in crossflow configuration with diameters from 0.5 mm to 2.0 mm. *International Journal of Heat and Mass Transfer, 98*, 448–454. https://doi.org/10.1016/j.ijheatmasstransfer.2016.02.072

Bejan, A. (1995). The optimal spacing for cylinders in crossflow forced convection. *Journal of Heat Transfer, 117*(3), 767–770. https://doi.org/10.1115/1.2822645

Bejan, A., Fowler, A. J., & Stanescu, G. (1995). The optimal spacing between horizontal cylinders in a fixed volume cooled by natural convection. *International Journal of Heat and Mass Transfer, 38*(11), 2047–2055. https://doi.org/10.1016/0017-9310(94)00312-J

Belegundu, A. D., & Chandrupatla, T. R. (2019). *Optimization concepts and applications in engineering* (3rd ed.). Cambridge: Cambridge University Press. https://doi.org/10.1017/9781108347976

Burden, F., & Winkler, D. (2008). Bayesian Regularization of Neural Networks. *Methods in Molecular Biology, 458*, 23–42. https://doi.org/10.1007/978-1-60327-101-1_3

Deng, Z., Wang, Z., Wang, Y., & Wan, L. (2024). Numerical simulation study on the resistance and heat transfer performance of anti-icing device of fin-staggered tube structure in marine intake system. *Applied Thermal Engineering, 244*, 122619. https://doi.org/10.1016/j.applthermaleng.2024.122619

Fang, Y., & Li, J. (2010). A Review of tournament selection in genetic programming. *Lecture Notes in Computer Science* (*including subseries Lecture Notes in Artificial Intelligence and Lecture Notes in Bioinformatics*), *6382*, 181–192. https://doi.org/10.1007/978-3-642-16493-4_19

Fausett, L. V., (2006). *Fundamentals of neural networks : architectures, algorithms, and applications*. Pearson Education India.

Ge, Y., Lin, Y., Tao, S., He, Q., Chen, B., & Huang, S. M. (2021). Shape optimization for a tube bank based on the numerical simulation and multi-objective genetic algorithm. *International Journal of Thermal Sciences, 161*, 106787. https://doi.org/10.1016/J.IJTHERMALSCI.2020.106787

Geb, D., Zhou, F., DeMoulin, G., & Catton, I. (2013). Genetic algorithm optimization of a finned-tube heat exchanger modeled with volume-averaging theory. *Journal of Heat Transfer, 135*(8). https://doi.org/10.1115/1.4024091/374862

Gu, L., Min, J., Wu, X., & Yang, L. (2017). Airside heat transfer and pressure loss characteristics of bare and finned tube heat exchangers used for aero engine cooling considering variable air properties. *International Journal of Heat and Mass Transfer, 108*, 1839–1849. https://doi.org/10.1016/j.ijheatmasstransfer.2017.01.047

Hoseinzadeh, S., Bahrami, A., Mirhosseini, S. M., Sohani, A., & Heyns, S. (2020). A detailed experimental airfoil performance investigation using an equipped wind tunnel. *Flow Measurement and Instrumentation*, *72*, 101717. https://doi.org/10.1016/j.flowmeasinst.2020.101717

Hoseinzadeh, S., & Heyns, P. S. (2020). Thermo-structural fatigue and lifetime analysis of a heat exchanger as a feedwater heater in power plant. *Engineering Failure Analysis, 113*, 104548. https://doi.org/10.1016/j.engfailanal.2020.104548

Karali, M. A., Almohammadi, B. A., Alshareef, R. S., Gad, A., Refaey, H. A., & Zied, K. (2025). Heat transfer enhancement and pressure drop from tube bank with splitter plates in cross flow employing RANS and LES turbulence models. *Thermal Science, (00)*, 26-26. https://doi.org/10.2298/TSCI241209026K

Kariman, H., Hoseinzadeh, S., Khiadani, M., & Nazarieh, M. (2023). 3D-CFD analysing of tidal Hunter turbine to enhance the power coefficient by changing the stroke angle of blades and incorporation of winglets. *Ocean Engineering, 287*, 115713. https://doi.org/10.1016/j.oceaneng.2023.115713

Khan, W. A., Culham, J. R., & Yovanovich, M. M. (2007). Optimal design of tube banks in crossflow using entropy generation minimization method. *Journal of Thermophysics and Heat Transfer, 21*(2), 372–378. https://doi.org/10.2514/1.26824

Kim, T. (2013). Effect of longitudinal pitch on convective heat transfer in crossflow over in-line tube banks. *Annals of Nuclear Energy, 57*, 209–215. https://doi.org/10.1016/J.ANUCENE.2013.01.060

Li, X., Zhu, D., Yin, Y., Tu, A., & Liu, S. (2019). Parametric study on heat transfer and pressure drop of twisted oval tube bundle within line layout. *International Journal of Heat and Mass Transfer, 135*, 860–872. https://doi.org/10.1016/j.ijheatmasstransfer.2019.02.031

Mainardes, R. L. S., Matos, R. S., Vargas, J. V. C., & Ordonez, J. C. (2007). Optimally staggered finned circular and elliptic tubes in turbulent forced convection. *Journal of Heat Transfer, 129*(5), 674–678. https://doi.org/10.1115/1.2712860

Mainardes, R. L. S., Matos, R. S., Vargas, J. V. C., & Ordonez, J. C. (2013). Pumping power minimization in staggered finned circular and elliptic-tube heat exchangers in turbulent flow. *Experimental Heat Transfer*, *26*(4), 397–411. https://doi.org/10.1080/08916152.2012.694011

Mashhadi, A., Sohankar, A., & Moradmand, M. M. (2024). Three-dimensional wake transition of rectangular cylinders and temporal prediction of flow patterns based on a machine learning algorithm. *Physics of Fluids*, *36*(9). https://doi.org/10.1063/5.0225180

Matos, R. S., Vargas, J. V. C., Laursen, T. A., & Saboya, F. E. M. (2001). Optimization study and heat transfer comparison of staggered circular and elliptic tubes in forced convection. *International Journal of Heat and Mass Transfer, 44*(20), 3953–3961. https://doi.org/10.1016/S0017-9310(01)00006-0

Matos, R. S., Vargas, J. V. C., Laursen, T. A., & Bejan, A. (2004a). Optimally staggered finned circular and elliptic tubes in forced convection. *International Journal of Heat and Mass Transfer, 47*(6–7), 1347–1359. https://doi.org/10.1016/J.IJHEATMASSTRANSFER.2003.08.015

Matos, R. S., Laursen, T. A., Vargas, J. V. C., & Bejan, A. (2004b). Three-dimensional optimization of staggered finned circular and elliptic tubes in forced convection. *International Journal of Thermal Sciences, 43*(5), 477–487. https://doi.org/10.1016/J.IJTHERMALSCI.2003.10.003

Mohanty, R. L., Swain, A., & Das, M. K. (2018). Thermal performance of mixed tube bundle composed of circular and elliptical tubes. *Thermal Science and Engineering Progress, 5*, 492–505. https://doi.org/10.1016/j.tsep.2018.02.009.

Naik, H., & Tiwari, S. (2021a). Thermodynamic performance analysis of an inline fin-tube heat exchanger in presence of rectangular winglet pairs. *International Journal of Mechanical Sciences, 193*, 106148. https://doi.org/10.1016/j.ijmecsci.2020.106148

Naik, H., & Tiwari, S. (2021b). Thermal performance analysis of fin-tube heat exchanger with staggered tube arrangement in presence of rectangular winglet pairs. *International Journal of Thermal Sciences, 161*. https://doi.org/10.1016/j.ijthermalsci.2020.106723.

Nazarieh, M., Kariman, H., & Hoseinzadeh, S. (2023). Numerical simulation of fluid dynamic performance of turbulent flow over Hunter turbine with variable angle of blades. *International Journal of Numerical Methods for Heat & Fluid Flow, 33*(1), 153-173. https://doi.org/10.1108/HFF-12-2021-0774

Rawa, M. J. H., Al-Turki, Y. A., Abu-Hamdeh, N. H., & Alimoradi, A. (2021). Multi-objective optimization of heat transfer through the various types of tube banks arrangements. *Alexandria Engineering Journal, 60*(3), 2905–2919. https://doi.org/10.1016/J.AEJ.2021.01.017.

Sahamifar, S., Kowsary, F., & Mazlaghani, M. H. (2019). Generalized optimization of cross-flow staggered tube banks using a subscale model. *International Communications in Heat and Mass Transfer, 105*, 46–57. https://doi.org/10.1016/j.icheatmasstransfer.2019.03.004

Shah, K., Patel, P., Mahant, K., & Yadav, C. O. (2013). CFD analysis of heat exchanger over a staggered tube bank for different angle arrangement of tube bundles. *International Journal of Engineering Research &*

Technology (IJERT), 2(1). https://www.ijert.org/research/cfd-analysis-of-heat-exchanger-over-a-staggered-tube-bank-for-different-angle-arrangement-of-tube-bundles-IJERTV2IS1445.pdf

Stanescu, G., Fowler, A. J., & Bejan, A. (1996). The optimal spacing of cylinders in free-stream cross-flow forced convection. *International Journal of Heat and Mass Transfer*, *39*(2), 311–317. https://doi.org/10.1016/0017-9310(95)00122-P.

Webb, R. L., & Kim, N. H. (2004). *Principles of enhanced heat transfer*. CRC Press; 2nd edition. https://doi.org/10.1201/b12413

Wilson, A. S., & Bassiouny, M. K. (2000). Modeling of heat transfer for flow across tube banks. *Chemical Engineering and Processing: Process Intensification, 39*(1), 1–14. https://doi.org/10.1016/S0255-2701(99)00069-0

Yilmaz, A., & Yilmaz, T. (2015). Optimum design of cross-flow in-line tube banks at constant wall temperature. *Heat Transfer Engineering, 37*(6), 523–534. https://doi.org/10.1080/01457632.2015.1060753.

Žukauskas, A. (1972). Heat Transfer from Tubes in Crossflow. *Advances in Heat Transfer, 8*(C), 93–160. https://doi.org/10.1016/S0065-2717(08)70038-8.